

# Radiative Auger Process in the Single Photon Limit on a Quantum Dot

Matthias C. Löbl,<sup>1,\*</sup> Clemens Spinnler,<sup>1</sup> Alisa Javadi,<sup>1</sup> Liang Zhai,<sup>1</sup> Giang N. Nguyen,<sup>2,1</sup> Julian Ritzmann,<sup>2</sup> Leonardo Midolo,<sup>3</sup> Peter Lodahl,<sup>3</sup> Andreas D. Wieck,<sup>2</sup> Arne Ludwig,<sup>2</sup> and Richard J. Warburton<sup>1</sup>

<sup>1</sup>*Department of Physics, University of Basel, Klingelbergstrasse 82, CH-4056 Basel, Switzerland*

<sup>2</sup>*Lehrstuhl für Angewandte Festkörperphysik, Ruhr-Universität Bochum, DE-44780 Bochum, Germany*

<sup>3</sup>*Niels Bohr Institute, University of Copenhagen, Blegdamsvej 17, Copenhagen DK-2100, Denmark*

In a multi-electron atom, an excited electron can decay by emitting a photon. Typically, the leftover electrons are in their ground state. In a radiative Auger process, the leftover electrons are in an excited state and a red-shifted photon is created<sup>1–3</sup>. In a quantum dot, radiative Auger is predicted for charged excitons<sup>4</sup>. For a singly-charged trion, a photon is created on electron-hole recombination, leaving behind a single electron. Radiative Auger determines the quantisation energies of this single electron, information which is otherwise difficult to acquire. For this reason, radiative Auger is a powerful tool. However, radiative Auger has not been observed on single quantum dots. Here, we report radiative Auger on trions in single quantum dots. There are sharp red-shifted emission lines with intensities as high as 1% of the main emission enabling the single-electron quantisation energies to be measured with high precision. Going beyond the original proposals, we show how quantum optics – an analysis of the photon correlations – gives access to the single-electron dynamics, notably relaxation and tunneling. All these properties of radiative Auger can be exploited on other semiconductor nanostructures and colour centres.

In an atom or a semiconductor, an excited electron can relax by the emission of a photon. The excited electron can also relax nonradiatively by the excitation of another electron – an Auger process<sup>5,6</sup>.

As originally pointed out by Felix Bloch, an Auger process can also take place together with a radiative transition<sup>3</sup>. In such a radiative Auger process, only part of the energy is transferred to another electron. The remaining energy goes to an emitted photon, which is correspondingly red-shifted. The radiative Auger process has been observed in X-ray spectra<sup>1,2</sup>. The so-called electron shake-off, which follows the beta-decay of a radioactive atom, has a similar physical origin<sup>7,8</sup>.

Nonradiative Auger processes involving continuum states have been observed in quantum dots<sup>9</sup>, two-dimensional materials<sup>10</sup>, color centers<sup>11</sup>, and are a major factor in determining the efficiency of semiconductor lasers<sup>12</sup>. At optical frequencies, Bloch's radiative Auger process has been described as a so-called shake-up process in the Fermi-sea<sup>13–15</sup>, a many-particle effect. In an atom-like configuration, the radiative Auger process has not been observed – neither in a few-electron configuration nor in the limit of a single-photon emitter. The prospect of applying quantum optics techniques to determine the dynamics of the electron following a radiative Auger process has not been considered so far.

Here, we measure the radiative Auger process at optical frequencies for the minimum number of two excited electrons. We observe the radiative Auger process for a negative trion (an exciton consisting of two electrons and one hole), which is confined to a zero-dimensional quantum dot (QD)<sup>4</sup>. Quantum optics techniques are used to prove that the strong fluorescence and the weak radiative Auger emission come from the same QD, and that the QD emits a photon either at the resonance frequency or at the radiative Auger frequency: the two colours cannot be created simultaneously and there is no time-ordering.

The radiative Auger process promotes the additional (Auger) electron to a higher shell of the QD. No continuum states are involved. The emitted photon is red-shifted by the energy which is transferred to the Auger electron. We show here that the radiative Auger effect is a powerful probe for single electrons: the energy separations between the resonance fluorescence and the radiative Auger emission directly measure the single-particle energies of the QD with a very high precision. In semiconductors, these single-particle energies are otherwise hard to access by optical means since particles are generally excited in pairs, as excitons. After the radiative Auger excitation, the Auger carrier relaxes back to the lowest shell of the confinement potential. With a quantum optics-based correlation measurement, we determine the rate corresponding to this single-particle relaxation in the absence of any other particles. Also this is typically hard to achieve by optical means: even for quasi-resonant  $p$ -shell excitation, electron relaxation takes place in the presence of a hole, which changes the relaxation dynamics.

We observe the radiative Auger process on two different systems: first, a self-assembled InGaAs QD in GaAs grown in the Stranski-Krastanov mode<sup>4</sup> and second, a GaAs QD in AlGaAs grown by infilling of droplet-etched nano-holes<sup>16</sup>. This system-independence strongly suggests that radiative Auger has general applicability: it allows precise, sensitive and fast optical techniques to determine the energies and dynamics of single electrons in semiconductor nanostructures.

We resonantly excite the negative trion ( $X^{1-}$ ) of a QD with a narrow-bandwidth laser. In both QD systems, the charge state of the QD is precisely controlled via Coulomb blockade<sup>17</sup>. We collect the emission of the QD and resolve it spectrally, as schematically shown in Fig. 1(a). Shown in Fig. 1(b) is the result of such a measurement for an InGaAs QD. The main peak at photon



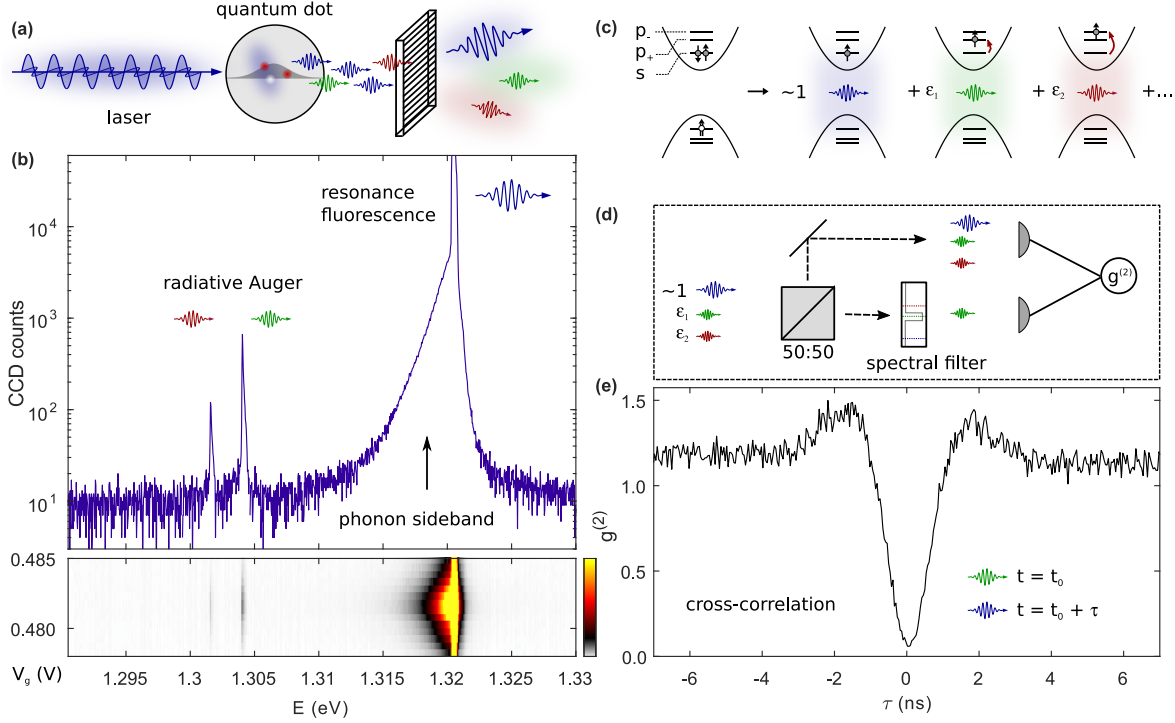


FIG. 1. **Observation of a radiative Auger process on a single quantum dot.** (a) Schematic of the experimental setup: the quantum dot (QD) is resonantly excited with a narrow-bandwidth laser, and its emission is spectrally resolved. (b) Emission spectrum of the negative trion ( $X^{1-}$ ) in an InGaAs QD under resonant excitation ( $T = 4.2$  K). The strong peak at  $E \simeq 1.321$  eV is the resonance fluorescence, which is surrounded by a broad LA-phonon sideband. Red-shifted by  $\hbar\omega_0 \sim 17$  meV there are two additional emission lines, stemming from the radiative Auger process. The QD can be tuned in and out of the resonance with the laser by exploiting the dc Stark effect via a gate voltage,  $V_g$ . The radiative Auger emission only appears when the QD is in resonance with the laser. (c) Mechanism of the radiative Auger process: with a probability close to one, the trion recombination results in an emission of a resonant photon and leaves the remaining electron in the ground state ( $s$ -shell). With small probabilities  $|\epsilon_1|^2$  and  $|\epsilon_2|^2$ , the remaining electron is promoted into one of the  $p$ -shells, and the photon is consequently red-shifted. (d) Setup for the cross-correlation between the radiative Auger emission and the resonance fluorescence. The delay  $\tau$  corresponds to the duration between the arrival of a resonant photon on detector 2 after the detection of an Auger photon on detector 1. (e) Cross-correlation measurement between the radiative Auger emission and the resonance fluorescence. The strong anti-bunching at zero time-delay proves that both emission lines originate from the same emitter.

energy  $\sim 1.321$  eV is the resonance fluorescence of the trion. This spectrally narrow emission is accompanied by an LA-phonon sideband on the red side<sup>18–20</sup>. The crucial observation we report here is the appearance of two weak emission lines, red-shifted by  $\sim 17$  meV from the main fluorescence peak. We show that these emission lines originate from a radiative Auger process, which is illustrated in Fig. 1(c): an electron and a hole recombine optically and with a small probability, the second electron is promoted to an excited state, the  $p$ -shell of the QD. In the case of resonance fluorescence, in contrast, the optical recombination of the trion leaves behind a single electron in the ground state ( $s$ -shell of the QD).

In the following, we prove that the red-shifted lines arise from a radiative Auger process. The evidence in the experiment is compelling based on a number of factors. First, the Auger lines disappear on removing the additional electron – they are absent in the emission spectrum of the neutral exciton,  $X^0$  (Supplement). Secondly, the

red-shifted emission lines only appear when the laser is in resonance with the QD (Fig. 1(b)). Thirdly, the time-resolved cross-correlation between the radiative Auger emission and the resonance fluorescence (Fig. 1(d,e)) shows a pronounced anti-bunching at zero time-delay. This quantum optics measurement proves that there is just one emitter, and that the emitter produces either a resonance-fluorescence photon or a radiative-Augur photon, but never two photons at the same time. Finally, to prove that the radiative Auger process leaves an electron in a higher shell, we measure the optical emission as a function of the magnetic field (Faraday geometry). The magnetic field creates an additional orbital confinement, which leads to a strong magnetic field dependence of higher QD-shells<sup>21–23</sup>. Therefore, also the radiative Auger emission should have a strong magnetic field dependence. This is exactly what we observe. The magnetic field dispersion of the radiative Auger emission is shown in Fig. 2(a,b) for an InGaAs QD and in Fig. 2(c,d)



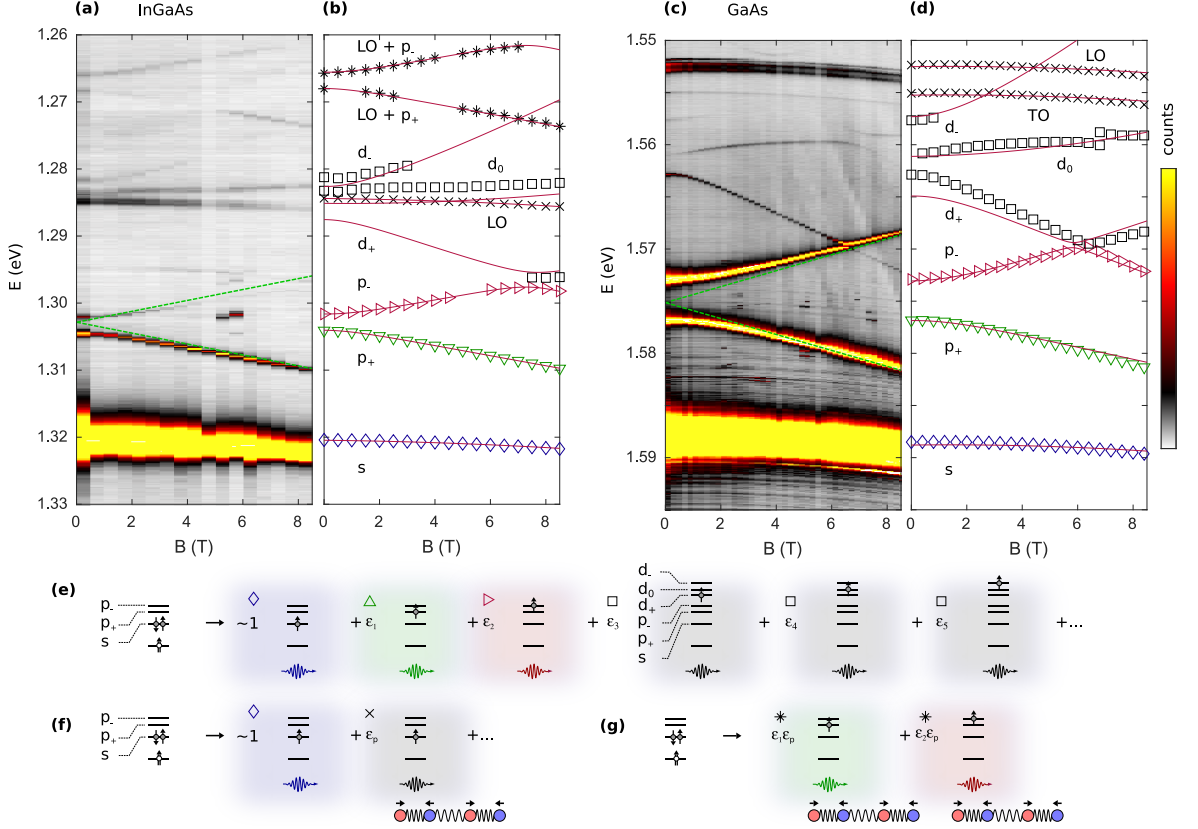


FIG. 2. **Magnetic field dispersion of the resonant Auger emission.** (a) Emission spectrum under resonant excitation as a function of the magnetic field measured on an InGaAs quantum dot (QD). The two green lines correspond to the radiative Auger emission where one electron is promoted into the  $p$ -shells. This emission follows a dispersion of  $\sim \pm \frac{1}{2} \hbar \omega_c$  (green lines) with  $m^* \simeq 0.071 m_e$  ( $\hbar \omega_0 \simeq 17.7$  meV, further parameters in the Supplement). (b) Magnetic field dispersion of the radiative Auger emission. The emission lines above the  $s$ -shell can be well described by the Fock-Darwin spectrum. The red lines represent a fit of our analytical model of the radiative Auger emission (see Supplement). (c) Radiative Auger emission as a function of the magnetic field measured on a GaAs QD ( $m^* \simeq 0.076 m_e$ ,  $\hbar \omega_0 \simeq 13.8$  meV). (d) Magnetic field dispersion of the radiative Auger emission for the GaAs QD. (e) Schematics of the radiative Auger process involving both  $p$ - and  $d$ -shells. (f) Optical recombination involving the creation of an LO- or a TO-phonon. We note that this process is observed for the trion and the neutral exciton (see Supplement). (g) Schematics of the radiative Auger process involving both carrier excitation to the  $p$ -shell and the creation of a phonon.

for a GaAs QD. At high magnetic fields, the two red-shifted emission lines, which are the closest in photon energy to the resonance-fluorescence, have a dispersion of  $\pm \frac{1}{2} \hbar \omega_c$  (cyclotron frequency:  $\omega_c = \frac{eB}{m^*}$ , electron effective mass  $m^*$ ). This strong magnetic field dispersion shows that the emission is connected to an energy transfer to the  $p$ -shells.

In this measurement, the separation between resonance fluorescence and radiative Auger emission corresponds to the single-particle energies. The radiative Auger lines, therefore, allow the single-particle spectrum of a quantum dot to be determined with very high precision. At zero magnetic field ( $B = 0$  T), there is a splitting between the two  $p$ -shell-related Auger lines, revealing an asymmetry of the QD. This asymmetry lifts the four-fold degeneracy of the  $p$ -shells into two doublets at zero magnetic field. For both types of QDs, we also observe radiative Auger emission involving  $d$ -shells (Fig. 2(e)).

At high magnetic fields, the upper  $p$ -shell ( $p_-$ ) shows an anti-crossing with the lowest  $d$ -shell ( $d_+$ ). For the GaAs QD, we even observe radiative Auger emission lines involving all three  $d$ -shells. For the InGaAs QD, the  $d_+$ -shell is only visible in the radiative Auger emission when it is coupled to the  $p_-$ -shell. For both types of QDs, the dispersion of the emission lines is quite well described by the Fock-Darwin spectrum. This shows that the confinement potential is close to harmonic.

For a rotationally symmetric confinement potential, angular momentum is a good quantum number such that promotion of the Auger electron to the  $d_0$  shell is possible, but promotion to the other  $p$ - and  $d$  shells is forbidden. In practice, we find that the radiative Auger involving the  $p$ -shells is relatively strong and that the intensity of these processes is not strongly dependent on the magnetic field. This shows that angular momentum is not a good quantum number in practice. However, in the



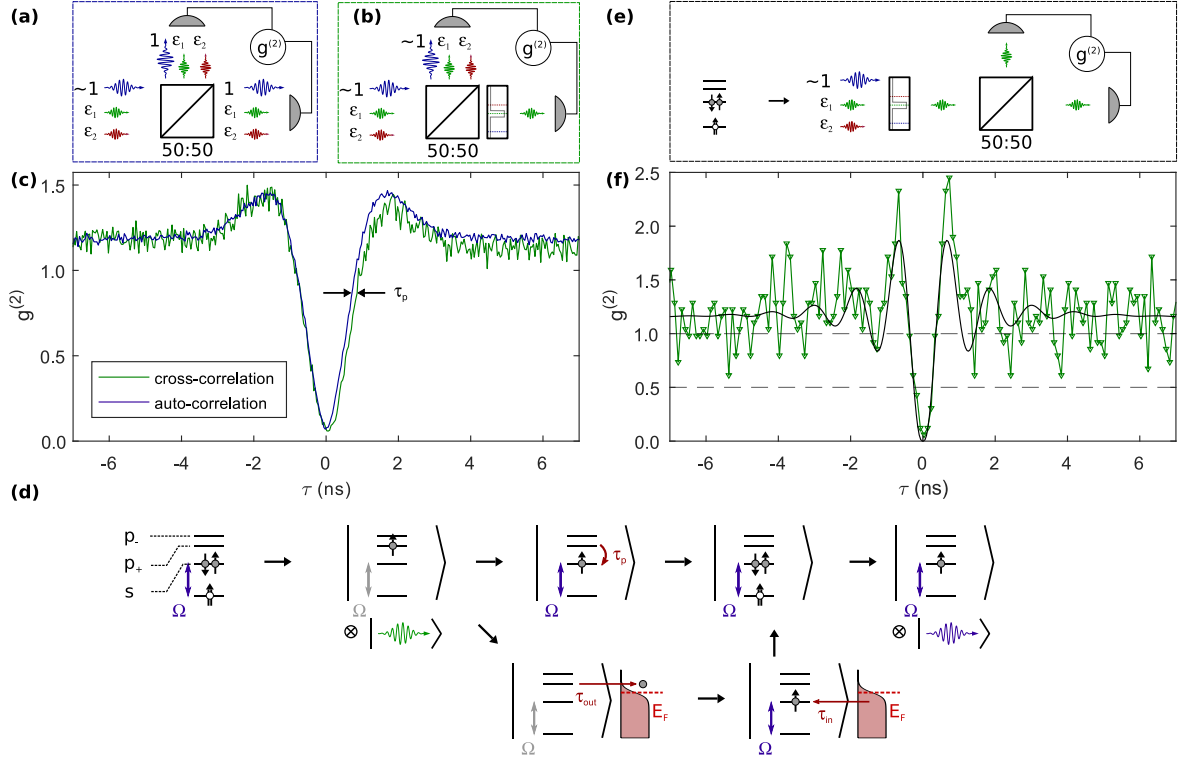


**FIG. 3. Time-resolved correlation measurements.** (a) Schematic of the measurement to determine the auto-correlation of the resonance fluorescence from a quantum dot (QD). The signal is split by a 50:50 beamsplitter; photon arrival times are recorded on two single-photon detectors ( $g^{(2)}$ -measurement). (b) Schematic of the cross-correlation measurement between resonance fluorescence and radiative Auger emission. The Auger emission is spectrally filtered to remove all resonant photons. (c) Cross-correlation between the resonance fluorescence and the radiative Auger emission (green). An auto-correlation of the resonance fluorescence (blue) is shown for comparison. A time offset of  $\tau_p \sim 85$  ps between the auto-correlation and the cross-correlation is a measure of the relaxation time of a single electron from the  $p$ - to the  $s$ -shell. (d) Mechanism: after the radiative Auger excitation, the second electron occupies the  $p$ -shell of the QD. When the electron occupies the  $p$ - rather than the  $s$ -shell, the Coulomb interactions are different, turning the  $s$ -to- $s$  transition out of resonance with the laser. The QD cannot be re-excited until the electron has relaxed to the  $s$ -shell. There are two relaxation channels: a direct relaxation to the  $s$ -shell on a time scale  $\tau_p$ ; and ionization of the QD by tunneling from the  $p$ -shell to the Fermi-reservoir of the back gate ( $\tau_{out}$ ) followed by slower tunneling from the Fermi reservoir to the  $s$ -shell ( $\tau_{in}$ ). After relaxation, the QD can be re-excited by the laser. (e) Schematic of the auto-correlation measurement of the radiative Auger emission. The radiative Auger signal is split and sent to two single-photon detectors. (f) Auto-correlation of the radiative Auger process involving the lower energy  $p$ -shell (green). The solid black line is a model where all parameters are identical to the simulation of the cross-correlation (see Supplement). The Rabi-frequency is higher compared to the cross-correlation measurement.

experiment all the processes are spin-conserving: we do not observe for instance Zeeman splittings in the radiative Auger lines. This shows that spin is a good quantum number; equivalently, that spin-orbit interactions of the electron states are weak.

There are several additional red-shifted emission lines that are not related to electron shells or continuum states (see Fig. 2(a,b)): An emission red-shifted by  $\sim 36$  meV corresponds to an optical recombination along with the creation of an LO-phonon (Fig. 2(f)). The magnetic field dispersion is weak and follows the QD  $s$ -shell – no higher QD-shells are involved. At lower photon energies, even the LO-phonon resonance of the radiative Auger emission is visible (Fig. 2(g)). In this case, Auger carrier excitation into  $p$ -shells and LO-phonon creation occur si-

multaneously with the optical recombination. The identification of these lines is confirmed by the magnetic field dispersion which equals the dispersion of the radiative Auger emission (see Fig. 2(b)).

We turn to the dynamics of the radiative Auger process, i.e. the dynamics of the electron left in an excited state following a radiative Auger process. Detecting a photon from a radiative Auger process projects the Auger electron into one of the excited electron states. The dynamics of this single electron can be investigated by determining the time of subsequent emission events. The experiment involves measuring the  $g^{(2)}(\tau)$  correlation function with high precision in the delay  $\tau$ . We compare the auto-correlation of the resonance fluorescence (Fig. 3(a)) to the cross-correlation between the radia-



tive Auger emission and the resonance fluorescence (Fig. 3(b)). This comparison provides immediate insight into the carrier relaxation mechanism following the radiative Auger process. The corresponding  $g^{(2)}$ -measurements are shown in Fig. 3(c).

The auto-correlation (blue curve) shows an anti-bunching at zero time delay, proving the single-photon nature of the resonance fluorescence. The anti-bunching at zero delay is surrounded by a bunching at a non-zero time delay. This effect is caused by the onset of Rabi-oscillations under strong resonant driving. The cross-correlation (green curve) differs from the auto-correlation in two main respects: The  $g^{(2)}(\tau)$  is a slightly asymmetric function of  $\tau$  and has a time-offset towards positive  $\tau$ . We explain these features following Fig. 3(d): After the emission of a radiative Auger photon, the second electron is located in a higher shell. Before re-excitation of the trion can take place, this electron has to relax down to the  $s$ -shell – in contrast to the resonance fluorescence where re-excitation is immediately possible. By comparing auto- and cross-correlation, we determine the relaxation time for an isolated electron to be  $\tau_p \simeq 85$  ps. The time-scale of the electron relaxation is comparable to numbers reported for weak nonresonant excitation<sup>24,25</sup>. The relaxation might be caused by a multi-phonon emission process<sup>26</sup>. We stress the advantage of the present method: the radiative Auger process leaves a single electron in a higher shell; the hole has disappeared; the chance of creating electrons or holes in continuum states is extremely small.

The asymmetry of the cross-correlation measurement can be explained by ionization of the QD following the radiative Auger emission. In a higher shell, the electron has an enhanced tunneling rate out of the QD<sup>27</sup>. Following very fast relaxation down to the Fermi-energy, tunneling back into the  $s$ -shell of the QD takes about 10 times longer, and the QD is ionized for a finite time. We estimate the corresponding tunneling times by modeling the auto- and cross-correlation measurements (see Supplement).

Finally, we perform the first auto-correlation measurement of the radiative Auger emission itself. For this measurement, all the resonance fluorescence is filtered out (Fig. 3(e)). To maximize the count rate of the weak radiative Auger emission, we use a higher Rabi-frequency compared to the cross-correlation measurement ( $\Omega_R = 5.4$  GHz). The auto-correlation measurement is shown in Fig. 3(f). At zero time delay, there is a clear anti-bunching in the  $g^{(2)}$ -measurement, which proves the single-photon nature of the emission connected to the radiative Auger process. At non-zero time-delay, the onset of Rabi-oscillations in the  $s$ -to- $s$  transition is visible as a photon bunching of the radiative Auger emission. Both features are well described by our model (see Supplement).

To explain the radiative Auger process, the Coulomb interactions between the carriers forming the trion must be considered. The radiative Auger process takes place

because these interactions change the eigenfunctions of the system (see Supplement). In a single-particle basis, the initial state contains admixtures of Slater-determinants of higher single-particle shells. The optical recombination removes an electron-hole pair from the initial trion state, leading to a final state which is a superposition of single-electron single-particle states. Every state in that superposition consists of an electron in a particular shell along with a photon of a certain energy. Since the initial state is always the same, the energy separations between the different emission lines correspond to precise single-particle splittings. The ratio of radiative Auger emission and resonance fluorescence reflects the expansion of the trion state in single-particle states. Compared to the resonance fluorescence, the radiative Auger emission is weaker by about 2-3 orders of magnitude. The trion wavefunctions are close, yet not equal to, single-particle states.

In conclusion, we experimentally demonstrate that there is a radiative Auger process connected to the optical recombination of a trion in a single QD. The measurements are performed on two different types of semiconductor QDs. We show how the radiative Auger process enables to determine the behaviour of a single-electron in the QD (energy quantization, relaxation and tunneling dynamics) using the precise, sensitive and fast tools of quantum optics. The radiative Auger process only requires significant Coulomb interactions within the trion, a very general feature. Therefore, this process should be observable for other quantum emitters in the solid-state.

## I. ACKNOWLEDGMENTS

We would like to thank Philipp Treutlein for fruitful discussions. MCL, CS, and RJW acknowledge financial support from NCCR QSIT and from SNF Project No. 200020.156637. LZ received funding from the European Union Horizon 2020 Research and Innovation programme under the Marie Skłodowska-Curie grant agreement No. 721394 (4PHOTON). JR, AL, and ADW gratefully acknowledge financial support from the grants DFH/UFA CDF A05-06, DFG TRR160, DFG project 383065199, and BMBF Q.Link.X 16KIS0867. LM and PL gratefully acknowledges financial support from the Danish National Research Foundation (Center of Excellence Hy-Q, grant number DNR F139) and the European Research Council (ERC Advanced Grant SCALE).

## II. AUTHOR CONTRIBUTIONS

MCL, CS, LZ, GNN, AJ performed the experiments. JR, ADW, and AL grew the samples. CS, MCL, LM fabricated the different samples. MCL, LZ, PL, AL designed the samples. MCL, CS, LZ, RJW analyzed the data. MCL developed the theory of the radiative Auger process. AJ, MCL, CS developed the theory for the time-



resolved measurements. MCL, RJW, CS developed the theory for the magnetic field dispersion. MCL and RJW initiated the project and wrote the manuscript with input from all the authors.

### III. METHODS

The samples are grown by molecular beam epitaxy. Sample A contains InGaAs QDs embedded in a *p-i-n-i-n*-diode structure<sup>28–31</sup>. Sample B contains GaAs QDs in AlGaAs, which are grown by GaAs-infilling of Al-droplet etched nano-holes<sup>16,32</sup>. The photon out-coupling is enhanced by a distributed Bragg mirror below the QDs. For both samples, the QDs are placed between a *p*-doped top gate and an *n*-type doped back gate. The QDs are tunnel-coupled to the back gate. This configuration stabilizes the charge environment of the QDs and enables tuning the QD charge state by applying a voltage between top and back gate<sup>33,34</sup>. For the InGaAs QDs, the back gate has a distance of 40 nm to the QDs, 30 nm for the GaAs QDs. In a magnetic field, there is optical spin-pumping in the center of the trion charge plateau<sup>35,36</sup>. Therefore, we perform all experiments at the plateau edges, where co-tunneling randomizes the electron spin<sup>37</sup>.

All time-resolved measurements are performed by using superconducting single-photon detectors. The overall timing resolution for the  $g^{(2)}$ -measurements is IRF  $\simeq$  35 ps (full width at half maximum). Optical measurements are carried out at 4.2 K in a helium bath cryostat. Resonant excitation of the QDs is performed with a narrow-bandwidth ( $\sim$  1 MHz) tunable diode laser (Topica DLpro), which is additionally filtered with a home-built grating setup in order to remove any background from the gain medium of the laser. Resonance fluorescence of individual QDs is measured by suppressing the reflected laser light with a cross-polarization technique.

### IV. MODELING THE MAGNETIC FIELD DISPERSION

The radiative Auger emission appears on resonantly exciting the trion. Fig. 4(a) shows a comparison of the emission spectrum from a neutral exciton and a trion. The emission spectrum of the neutral exciton ( $X^0$ ) only shows phonon-related features. A radiative Auger emission is impossible for the  $X^0$  due to the absence of an Auger electron.

The final states after the optical recombination of the trion are single-particle states. Therefore, the separations between the different emission lines are precise single-particle energies. Shown in Fig. 4(b,c) is the magnetic field dispersion of the extracted single-particle energies for two different QDs. Fig. 4(d,e) shows the single-particle dispersion for the two QDs shown in the main text. We measure an *s*-to-*p*-splitting of 17.7 meV respectively 21.0 meV on the InGaAs QDs; and 13.8 meV

respectively 17.6 meV on the GaAs QDs. We can determine many further parameters of the single-particle spectrum by fitting the data to a model which assumes states of an asymmetric harmonic confinement potential. The red lines in Fig. 4(b-e) represent the model that is developed in this section. It reproduces the data very well.

For a symmetric two-dimensional confinement potential, the magnetic field dependence of the single-particle states forms the Fock-Darwin spectrum<sup>22,23</sup>. The eigenenergies  $E_{n,L}$  depend on two quantum numbers, the radial quantum number,  $n$ , and the angular momentum quantum number,  $L$ <sup>21</sup>. In this model, the two *p*-shells are degenerate at zero magnetic field. This is clearly not the case in our experiments. To describe the single-particle dispersions, we therefore assume an asymmetric harmonic confinement potential of the form  $V(x, y) = \frac{1}{2}m_e^*(\omega_x^2x^2 + \omega_y^2y^2)$ . When the radial symmetry is broken, angular momentum is no longer a good quantum number, and the eigenenergies are  $E_{n_x, n_y} = \hbar\omega_x(n_x + \frac{1}{2}) + \hbar\omega_y(n_y + \frac{1}{2})$ , with the two quantum numbers  $n_x$  and  $n_y$ . The eigenenergies of such an asymmetric harmonic confinement as a function of the magnetic field are given in Ref. 38.

The absolute energies of the emission lines correspond to the energy differences between the initial state and the final states. To fit the dispersions of these emission lines, we compute the energy of the initial trion state as the sum of its single-particle energies plus the corresponding Coulomb and exchange terms. For the Coulomb energy terms, we assume a symmetric confinement as the corresponding energy terms can be easily computed analytically<sup>39–41</sup>. Coupling terms admixing higher shells are not considered in this estimation<sup>39,40</sup>.

At a magnetic field of  $B \simeq 8$  T, the *p*<sub>-</sub> and the *d*<sub>+</sub>-shells anticross. This is not a feature of the energy spectrum of an asymmetric harmonic oscillator. The anti-crossing is included by a phenomenological coupling  $\Delta_{pd}$  between *p*<sub>-</sub> and *d*<sub>+</sub>-shell. We speculate that the coupling between both shells arises due to the deviation from a harmonic confinement.

When part of the energy is transferred to an LO-phonon, the corresponding photon energy is given by,  $E_{\text{trion}} - E_f^s - \Delta_{LO}$ . This emission has the same weak magnetic field dependence as the resonance fluorescence (*s*-shell emission).

The results of fitting our model are shown in Fig. 4 and Fig. 2 of the main text. A list of definitions is given in Tab. IV, and the fit parameters are given in Tab. II. For all measured QDs, the strong magnetic field dispersion of the radiative Auger emission lines is excellently reproduced by this description.

In the case of the InGaAs QD shown in Fig. 2(a,b) (main text), we fit the energies of the *s*-shell emission and the radiative Auger emission into both *p*-shells simultaneously. The coupling term  $\Delta_{pd}$  is included as a fit parameter. The exciton *g*-factor is measured independently by mapping out the charge plateau of the trion



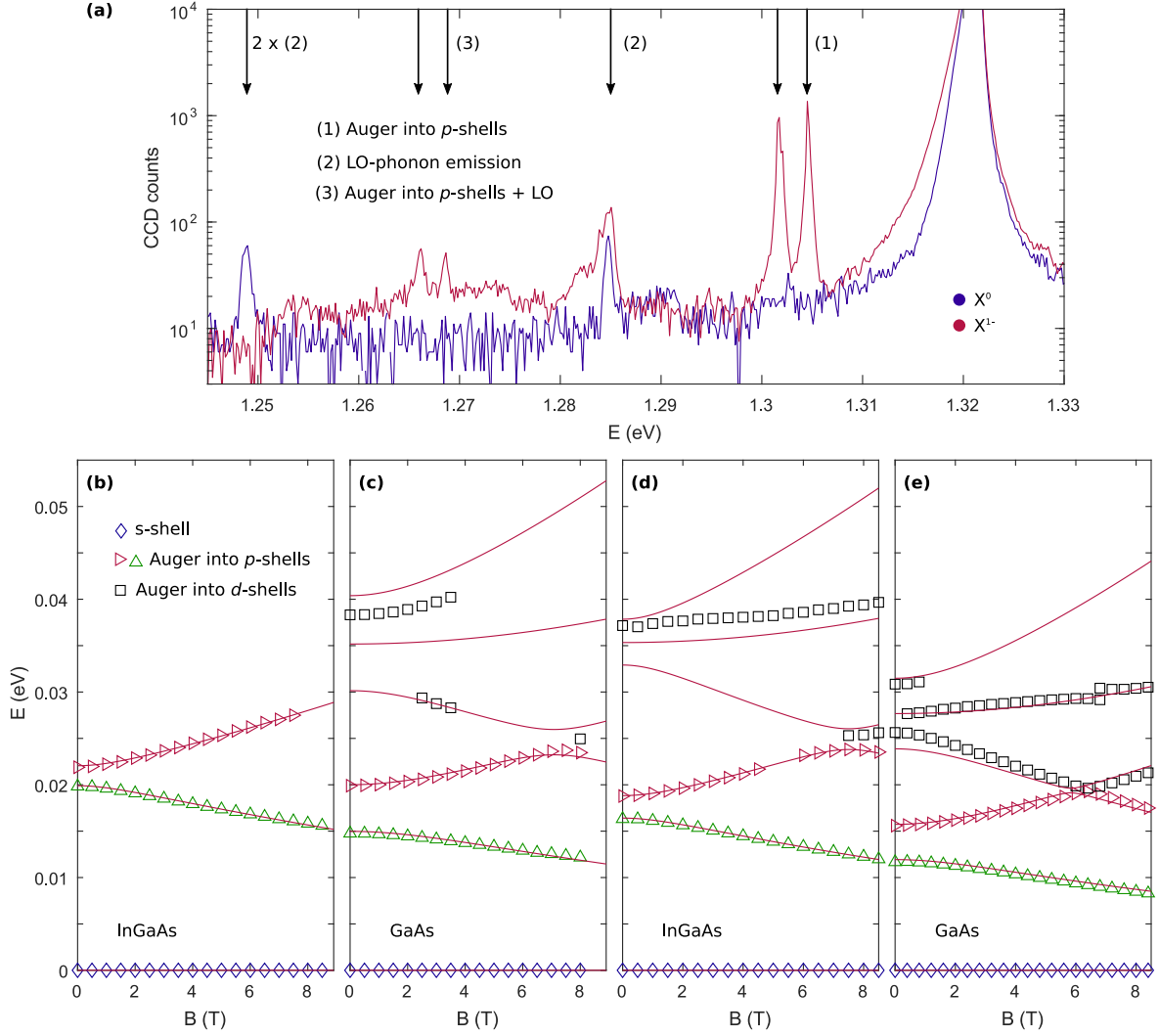


FIG. 4. **(a)** Emission spectrum of the InGaAs quantum dot shown in Fig. 2(a) in the main text. The  $s$ -to- $s$  transition of the QD is resonantly excited. The emission is shown for the neutral exciton ( $X^0$ ) and the singly charged trion ( $X^{1-}$ ). For better comparability, the neutral exciton ( $X^0$ ) is shifted in energy such that its resonance fluorescence peak overlaps with the charged exciton ( $X^{1-}$ ). In both cases, the resonance fluorescence (at  $E \simeq 1.321$  eV) dominates. Emission at lower energies is caused by an energy transfer to either an LO-phonon or an additional carrier via the radiative Auger process. The radiative Auger process is only possible for the trion, not for the neutral exciton. **(b)** Single-particle magnetic field dispersion for another InGaAs QD. To obtain the single-particle energies, the  $s$ -shell energy is subtracted from the energies of the radiative Auger lines. **(c)** Single-particle magnetic field dispersion for another GaAs QD embedded in AlGaAs. **(d)** Single-particle energies for the QD shown in Fig. 2(a) of the main text. **(e)** Single-particle energies for the QD shown in Fig. 2(c) of the main text.

in a magnetic field. The fit reproduces the data very well and gives a good description of the radiative Auger excitation into some of the  $d$ -shells. The LO-phonon resonance of the radiative Auger excitation into the  $p$ -shells is also excellently reproduced by the fit.

To fit the magnetic field dispersion of the InGaAs QD shown in Fig. 4(b), we also make a simultaneous fit to the energies of the  $s$ -shell emission and the radiative Auger emission into both  $p$ -shells. The coupling term  $\Delta_{pd}$  is not included as there is no hint of an anticrossing with the  $d_+$ -shell.

For the GaAs QD shown in Fig. 2(c,d) of the main

text, we again fit the energies of the  $s$ -shell emission and the radiative Auger emission into both  $p$ -shells simultaneously. The coupling term  $\Delta_{pd}$  is included as a fit parameter. The exciton  $g$ -factor is measured independently and not fitted.

For the GaAs QD shown in Fig. 4(c), we again fit the energies of the  $s$ -shell emission and the radiative Auger emission into both  $p$ -shells simultaneously. The exciton  $g$ -factor is fixed to a value typical for GaAs QDs.

When observable, all phonon-related features are described using the fit results described above. A constant phonon energy is used as a single fit parameter.



label	description
$\hbar$	reduced Planck constant
$\mu_B$	Bohr magneton
$\epsilon_0, \epsilon_r$	permittivity of vacuum, relative permittivity
$g_e, g_h$	electron and hole g-factor
$E_0$	bandgap of the QD-material
$m_e^*, m_h^*$	electron, hole effective mass
$\hbar\omega_c = \frac{\hbar e B}{m_e^*}$	electron cyclotron energy
$\hbar\omega_x, \hbar\omega_y$	confinement energies of the asymmetric harmonic oscillator
$\hbar\omega_0 \equiv \hbar\omega_x + \Delta_p \equiv \hbar\omega_y - \Delta_p$	confinement energy of the symmetric harmonic oscillator
$n, L$	quantum numbers for the symmetric harmonic oscillator
$n_x, n_y$	quantum numbers for the asymmetric harmonic oscillator
$E_{n,L}$	eigenenergies of the symmetric harmonic oscillator
$E_{ij}^e, E_{ij}^h$	Coulomb energy between two electrons and two holes in the shells $i, j$
$X_{ij}^e, X_{ij}^h$	exchange Coulomb energy between an electron/hole in the shells $i, j$
$\Delta_{pd}$	coupling between $p_-$ - and the $d_+$ -shell
$\Omega_R$	Rabi frequency
$\Gamma_r = \tau_r^{-1}$	radiative decay rate
$\Gamma_A = \tau_A^{-1}$	radiative Auger decay rate.
$\Gamma_p = \tau_p^{-1}$	relaxation rate from $p$ - to $s$ -shell
$\Gamma_{\text{out}} = \tau_{\text{out}}^{-1}$	tunnel rate out of the QD after a radiative Auger decay
$\Gamma_{\text{in}} = \tau_{\text{in}}^{-1}$	tunnel rate into the ionized QD
$E_f^{p\pm}, E_f^{d\pm}, \text{ and } E_f^{d_0}$	final state energies after Auger excitation into $p$ - and $d$ -shells
$\Delta_{LO}, \Delta_{TO}$	energies of longitudinal and transverse optical phonon

TABLE I. List of definitions.

	$E_0$ (eV)	$m_e^* (m_0)$	$g_h - g_e$	$\hbar\omega_0$ (meV)	$\Delta_p$ (meV)	$\Delta_{pd}$ (meV)	$\Delta_{LO}$ (meV)	$\Delta_{TO}$ (meV)
InGaAs, Fig. 2(b) (main text)	1.3214	0.0712	1.505	17.67	1.26	1.12	36.1	–
GaAs, Fig. 2(d) (main text)	1.5925	0.0757	1.135	13.84	1.90	0.25	36.3	33.5
InGaAs, Fig. 4(b)	1.3152	0.0762	1.968	20.98	1.08	–	–	–
GaAs, Fig. 4(c)	1.5757	0.0737	1.1	17.59	2.61	1.37	36.5	–

TABLE II. Fit results for the magnetic field dispersion.

## V. RADIATIVE AUGER PROCESS: THEORY

To find the multi-particle eigenstates,  $\{\Psi_{\mathbf{n}}\}$ , of several carriers in the same QD, we numerically solve the time-independent Schrödinger equation,  $\hat{H}\Psi = E\Psi$ , via exact diagonalization. The index  $\mathbf{n}$  is the set of quantum numbers required to describe all particles. The Hamiltonian,  $\hat{H}$ , of the system is:

$$\hat{H} = \sum_{i=1}^N \left[ \frac{-\hbar^2}{2m_i^*} \Delta_i + V(\vec{x}) \right] + \hat{C}. \quad (1)$$

$\hat{C}$  is the Coulomb operator, which is given by:

$$\hat{C} = \frac{1}{4\pi\epsilon_0\epsilon_r} \sum_{i,j, i \neq j}^N \frac{c_i \cdot c_j}{|r_i - r_j|}. \quad (2)$$

The term  $c_i = \pm e$  is the charge of a particle (electron or hole). As we are considering fermionic particles, the overall wavefunction is antisymmetric under particle exchange. Therefore, we consider  $\hat{H}$  in a basis of antisymmetrized Slater determinants:

$$\Psi_{\mathbf{n}} = \hat{\mathcal{A}} \prod_{i=1}^N \phi_{n_i}(x_i, \sigma_i). \quad (3)$$

These Slater determinants are constructed from the single-particle solutions,  $\phi_{n_i}(x_i, \sigma_i)$ , of Eq. 1. The asymmetrization operator,  $\hat{\mathcal{A}}$ , constructs a Slater-determinant, which is asymmetric under the exchange of identical particles. To express  $\hat{H}$  in the basis  $\{\Psi_{\mathbf{n}}\}$ , the matrix elements  $\langle \Psi_{\mathbf{n}} | \hat{H} | \Psi_{\mathbf{m}} \rangle$  have to be computed. The Slater-Condon rules<sup>42,43</sup> transform these multi-particle matrix elements into two-particle Coulomb matrix elements. The Slater-Condon rules for the two-particle



Coulomb operator,  $\hat{C}$ , are:

$$\langle \Psi_{\mathbf{n}} | \hat{H} | \Psi_{\mathbf{n}} \rangle = \frac{1}{2} \sum_{i, j, i \neq j}^N [V_{ijij} - V_{ijji}] \quad (4)$$

$$\langle \Psi_{\mathbf{n}} | \hat{H} | \Psi_{\mathbf{n}(h,k)} \rangle = \sum_{i=1}^N [V_{hiki} - V_{hiik}] \quad (5)$$

$$\langle \Psi_{\mathbf{n}} | \hat{H} | \Psi_{\mathbf{n}(h,k,l,m)} \rangle = V_{hlkm} - V_{hlmk}. \quad (6)$$

The index  $\mathbf{n}(h,k)$  indicates that this wavefunction has been obtained by replacing the single-particle wavefunction  $\phi_h$  of particle number  $h$  by  $\phi_k$ . The index  $\mathbf{n}(h,k,l,m)$  means that two wavefunctions are changed correspondingly. The two-particle Coulomb matrix elements,  $V_{hklm}$ , are given by the following integral:

$$\begin{aligned} V_{hklm} &= \langle \phi_h \phi_k | \hat{C} | \phi_l \phi_m \rangle \\ &\equiv \frac{e^2}{4\pi\epsilon_0\epsilon_r} \int \int \frac{\phi_h(\mathbf{r}_1)^* \phi_k(\mathbf{r}_2)^* \phi_l(\mathbf{r}_2) \phi_m(\mathbf{r}_1)}{|\mathbf{r}_1 - \mathbf{r}_2|} d\mathbf{r}_1 d\mathbf{r}_2. \end{aligned} \quad (7)$$

Depending on the order of the indices, these integrals include the direct Coulomb and the Coulomb exchange terms. For a symmetric harmonic confinement potential, analytic solutions for the Coulomb integrals can be found e.g. in Refs. 39 and 40.

The eigenfunctions of Eq. 1 are obtained by diagonalizing  $\hat{H}$  in the basis  $\{\Psi_{\mathbf{n}}\}$ . The trion ground state has a small admixture of higher single-particle shells, which is the origin of the radiative Auger process. Upon optical recombination of one electron and a hole, the remaining electron of the trion is in a superposition including these higher shells. Detection of the frequency of the emitted photon projects the state of the remaining electron to the corresponding shell. For the trion, it is sufficient to carry out exact diagonalization for the initial state only since the final states are single-particle states.

In the dipole approximation, the emission spectrum can be computed with Fermi's golden rule<sup>44</sup>:

$$I(\omega) = \sum_f |\langle \Psi_{\mathbf{n}}^{(f)} | \hat{P} | \Psi_{\mathbf{n}}^{(i)} \rangle|^2 \cdot \delta(E_i - E_f - \hbar\omega), \quad (8)$$

where  $\Psi_{\mathbf{n}}^{(i)}$  is the initial state,  $\Psi_{\mathbf{n}}^{(f)}$  are the possible final states.  $\hat{P} = \sum \hat{h}_{i,\sigma} \hat{e}_{j,-\sigma}$  adds up all dipole allowed electron-hole recombinations<sup>44</sup>.

With the presented formalism, we estimate that the intensity of the radiative Auger transition from  $s$ - to the  $d_0$ -shell is about hundred times weaker than the resonance fluorescence. However, this intensity is tendentially overestimated compared to the experimentally obtained values. The issue could be that the exact diagonalization only converges when taking into account very high single-particle shells. In reality, not all of these states exist due to close-by continuum states.

## VI. CROSS-CORRELATION: THEORY

The  $g^{(2)}$ -measurements are modeled with the level scheme shown in Fig. 6. There are 4 different states which are taken into account for our simulation: the ground state,  $|g\rangle$ , with a single electron in the QD; the excited state,  $|e\rangle$ , a trion with two  $s$ -shell electrons; the state after a radiative Auger emission,  $|p\rangle$ , where a single electron occupies the  $p$ -shell of the QD; and the ionized QD-state,  $|b\rangle$ , where the electron has tunneled out of the QD. We simulate the system by assuming the Hamiltonian ( $\hbar = 1$ ):

$$\hat{H} = \frac{\Omega}{2} (|g\rangle \langle e| + |e\rangle \langle g|). \quad (9)$$

All decay channels are modeled following the scheme shown in Fig. 6. The Lindblad operator is:

$$\hat{\mathcal{L}} = \sqrt{\Gamma_r} |g\rangle \langle e| + \sqrt{\Gamma_A} |p\rangle \langle e| + \sqrt{\Gamma_p} |g\rangle \langle p| \quad (10)$$

$$+ \sqrt{\Gamma_{\text{out}}} |b\rangle \langle p| + \sqrt{\Gamma_{\text{in}}} |g\rangle \langle b|. \quad (11)$$

We compute the steady-state density matrix,  $\rho_s$ , and obtain the auto- and cross-correlation by using the Quantum Toolbox in Python (QuTiP<sup>45</sup>). The operator for the resonant decay is  $\hat{a} = \sqrt{\Gamma_r} |g\rangle \langle e|$ , and the operator for the radiative Auger decay is  $\hat{a}_A = \sqrt{\Gamma_A} |p\rangle \langle e|$ . Auto- and cross-correlations are computed numerically by applying the quantum regression theorem. The auto-correlation of the resonance fluorescence is given by:

$$g^{(2)}(\tau) = \frac{\langle \hat{a}^\dagger(t) \hat{a}^\dagger(t+\tau) \hat{a}(t+\tau) \hat{a}(t) \rangle}{\langle \hat{a}^\dagger(t) \hat{a}(t) \rangle^2}. \quad (12)$$

The cross-correlation is given by:

$$g^{(2)}(\tau) = \frac{\langle \hat{a}_A^\dagger(t) \hat{a}^\dagger(t+\tau) \hat{a}(t+\tau) \hat{a}_A(t) \rangle}{\langle \hat{a}^\dagger(t) \hat{a}(t) \rangle \langle \hat{a}_A^\dagger(t) \hat{a}_A(t) \rangle}. \quad (13)$$

The auto-correlation of the radiative Auger emission is:

$$g^{(2)}(\tau) = \frac{\langle \hat{a}_A^\dagger(t) \hat{a}_A^\dagger(t+\tau) \hat{a}_A(t+\tau) \hat{a}_A(t) \rangle}{\langle \hat{a}_A^\dagger(t) \hat{a}_A(t) \rangle^2}. \quad (14)$$

We multiply the result of this simulation by  $1 + c_1 \cdot \exp(-|\tau|/t_{bl})$  to take into account a weak blinking on short time-scales<sup>46</sup>, which might be caused by electron spin pumping enabled by a weak nuclear magnetic field<sup>47</sup>. Additionally, the model function is multiplied with a global prefactor  $c_0$ , which takes into account a weak blinking on a time-scale of  $\sim 0.1$  ms, probably caused by charge noise. For the resonance fluorescence, a small fraction  $c_l$  of reflected laser in the resonant emission is taken into account via  $g^{(2)} \rightarrow g^{(2)} \cdot (1 - c_l) + c_l$ . We perform a simultaneous fit of this model to the auto-correlation of the resonance fluorescence and the cross-correlation between the resonance fluorescence and the radiative Auger emission. The result of this fit is shown in Fig. 5. The



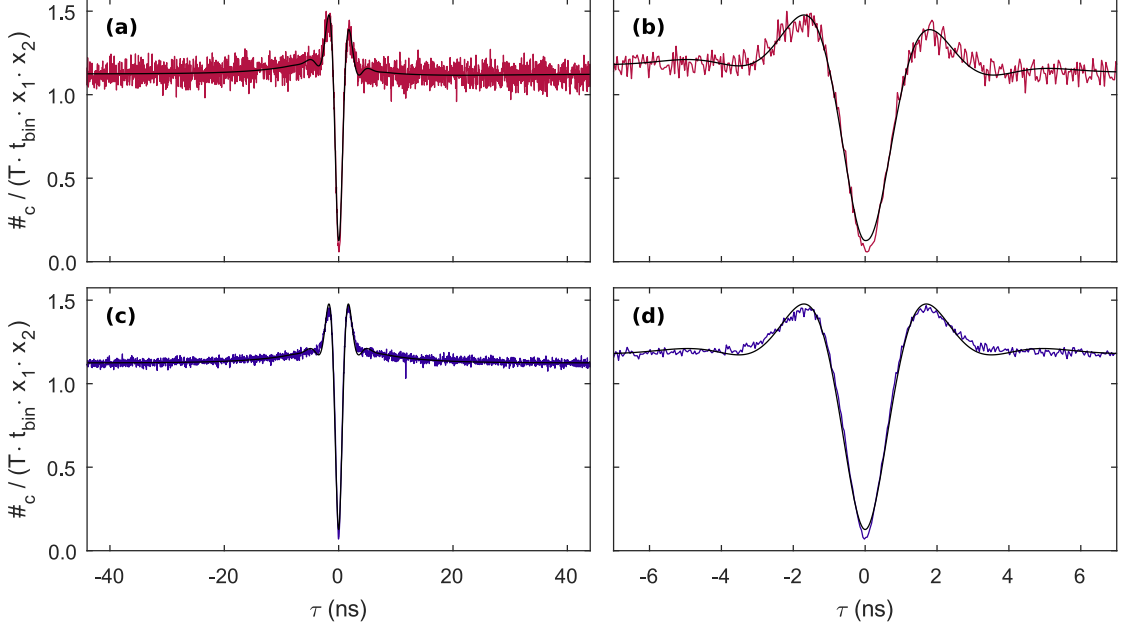


FIG. 5. Fits to the  $g^{(2)}$ -measurements shown in Fig. 3(c) of the main text. Simultaneous fitting of Eqs. 12 and 13 to the corresponding auto- and cross-correlation data is performed. In the following sub-figures, the black lines correspond to the fit result. **(a)** Red line: cross-correlation measurement between resonance fluorescence and the radiative Auger emission where the second electron is transferred into the  $p_+$ -shell of the quantum dot. **(b)** Cross-correlation measurement from (a) on a shorter time-scale. **(c)** Blue line: auto-correlation measurement of the resonance fluorescence. **(d)** Auto-correlation measurement from (c) on a shorter time-scale.

obtained fit parameters are stated in Tab. III. These parameters also give a good fit to the auto-correlation of the radiative Auger emission, which is shown in Fig. 3(f) of the main text. All fit parameters are kept the same, and only the Rabi-frequency is increased, taking into account that the auto-correlation of the radiative Auger emission has been measured at higher power.

## VII. EVALUATION OF CORRELATION MEASUREMENTS

All  $g^{(2)}$ -measurements are performed in a time-tagged, time-resolved mode. The arrival times of all photons are recorded over the full integration time,  $T$ , on two single-photon detectors. Any analysis is carried out post-measurement. We compute the cross-correlation ( $g^{(2)}$ ) between both signals by counting the coincidence events between the two detectors as a function of a time delay,  $\tau$ , between the signals.

Let  $x_1, x_2$  be the count rates on detector 1 and 2, respectively. We divide the full integration time into time-intervals of length,  $t_{bin}$ . The value for  $t_{bin}$  is chosen to be small enough such that the probability of a photon in the corresponding time-interval is very small:  $t_{bin} \cdot x_{1/2} \ll 1$ . For each detector, we can assign a number (0 for no photon or 1 for one photon in the interval) to every interval since the probability of having more than

one photon in the interval is negligibly small. We denote  $\#_c$  the number of coincidences for a fixed time delay. The cross-correlation between both detectors is obtained by dividing  $\#_c$  by its expectation value for the case of two uncorrelated detection channels:  $\langle \#_c \rangle = T \cdot t_{bin} \cdot x_1 \cdot x_2$ . This expression for  $\langle \#_c \rangle$  is obtained by the following consideration. The probability of finding a 1-event (photon) in a certain time interval is  $t_{bin} \cdot x_1$  and  $t_{bin} \cdot x_2$ . If both detection channels are uncorrelated, the probability of finding a 1-event for the first detector at time  $t$  and a 1-event for the second detector in the time-interval at  $t + \tau$  is  $p_c = t_{bin}^2 \cdot x_1 \cdot x_2$ . For  $T \gg \tau$ , the probability density distribution of  $\#_c$  is thus a binomial distribution:

$$P(\#_c) = \binom{T/t_{bin}}{\#_c} \cdot (1 - p_c)^{T/t_{bin} - \#_c} \cdot p_c^{\#_c} \quad (15)$$

The expectation value of this distribution is the corresponding normalization factor:  $\langle \#_c \rangle = T \cdot t_{bin} \cdot x_1 \cdot x_2$ .

## VIII. POWER DEPENDENT EXCITATION

We measure the intensity of the radiative Auger emission as a function of resonant excitation power and laser detuning. This measurement is shown in Fig. 7. In a first measurement, we keep the narrow-band laser at fixed frequency and sweep the detuning between trion transition and laser by applying a gate voltage,  $V_g$ . The gate



$\Omega$ (GHz)	$\Gamma_r$ (GHz)	$\Gamma_A$ (GHz)	$\Gamma_p$ (GHz)	$\Gamma_{out}$ (GHz)	$\Gamma_{in}$ (GHz)	$t_{bl}$ (ns)	$c_0$	$c_1$	$c_l$
1.85	1.22	0.001	11.7	0.82	0.07	7.2	1.143	0.153	0.126

TABLE III. Parameters obtained from simultaneously fitting the auto- and cross-correlation measurements shown in Fig. 5. The radiative decay rate,  $\Gamma_r$ , is obtained from a different measurement and is not included in the fit.  $\Gamma_A$  is estimated from the intensity ratio between radiative Auger emission and resonance fluorescence and is also not included in the fit.

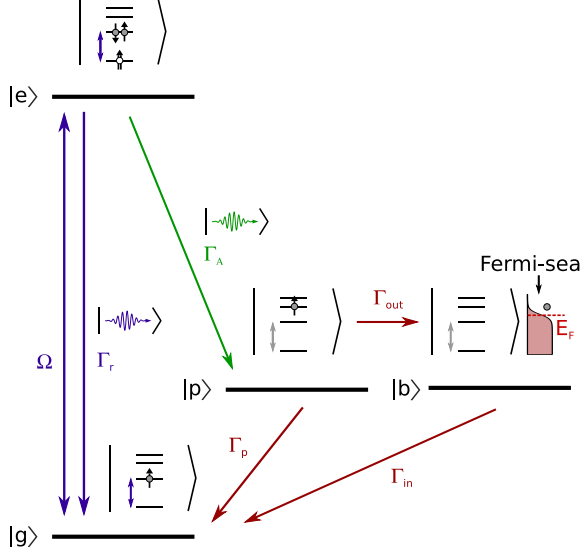


FIG. 6. Model used for the simulation of the auto-correlation measurement of the resonance fluorescence together with the cross-correlation between the resonance fluorescence and the radiative Auger emission.

voltage shifts the trion energy via the quantum-confined Stark effect. The intensity and the energy of the emission are recorded on a spectrometer. This measurement is shown in Fig. 7(a). When laser and trion energy are on resonance, there is a bright emission at  $\sim 1.321$  eV, the resonance fluorescence. This emission is spectrally asymmetric due to the LA-phonon sideband around the resonant peak. At lower energy,  $\sim 17$  meV below the resonance fluorescence, there is the emission corresponding to the radiative Auger excitation into the  $p$ -shells. This emission is strongest when also the resonance fluorescence is at its maximum, indicating that the intensity of the radiative Auger emission is proportional to the excited state population of the QD. Our model of the radiative Auger process implies this proportionality since the process only takes place in the excited state (trion) of the QD.

To investigate this dependence further, we keep the laser on resonance with the trion and measure the emission intensities as a function of power. This measurement is shown in Fig. 7(b). The power dependence of the resonance fluorescence and the radiative Auger emission follows the power saturation curve of a two-level system very well. This result also confirms that the radiative

Auger process is entirely related to the trion. Its rate is proportional to the trion occupation under resonant excitation<sup>48</sup>:

$$\Gamma_A \propto \rho_{22} = \frac{1}{2} \frac{\Omega_R^2}{2\Gamma_r^2 + \Omega_R^2}. \quad (16)$$

We expect that the ratio of the radiative Auger emission and resonance fluorescence intensities roughly reflects the ratio  $\Gamma_A/\Gamma_r$ . We estimate values for  $\Gamma_A$  to be on the order of  $\sim 1$  MHz.

Finally, we measure the linewidth of the radiative Auger emission. We pass the emission through a Fabry-Perot cavity (15.2 GHz free spectral range, 0.41 GHz linewidth) and sweep the cavity length. The result of this measurement on the  $p_+$ -emission is shown in Fig. 8(a). We determine the linewidth of the radiative Auger emission by fitting a multi-Lorentzian which is convoluted with the cavity linewidth. At low power, we measure a minimum linewidth of 4.19 GHz. For comparison,

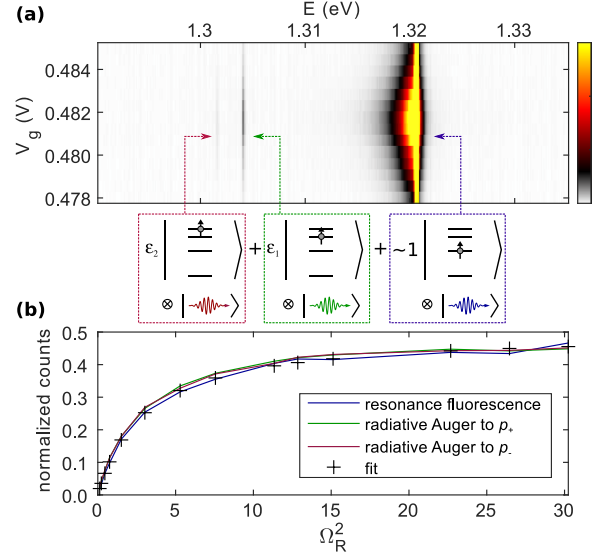


FIG. 7. (a) Resonance fluorescence and radiative Auger emission. The excitation laser is fixed ( $E \simeq 1.321$  meV), and the QD is swept through the resonance by tuning the gate voltage,  $V_g$ . (b) Dependence of resonance fluorescence and radiative Auger emission on the power of the resonant laser. For the power dependence, the laser is kept on resonance with the trion ( $X^{1-}$ ). When normalized, the resonance fluorescence and the radiative Auger emission intensity depend equally on the excitation power. Both are proportional to the upper state occupation of a resonantly driven two-level system.



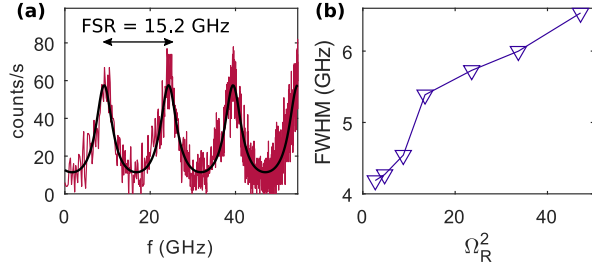


FIG. 8. (a) Radiative Auger emission at  $\Omega_R = 0.73$  GHz transmitted through a 0.41 GHz Fabry-Perot cavity. (b) Linewidth of the radiative Auger emission as a function of the resonant Rabi frequency.

the lifetime limited linewidth is estimated by the decay rate of the  $p_+$ -state after the radiative Auger process:  $\frac{\Gamma_r}{2\pi} = 1.99$  GHz. We repeat the linewidth measurement for different excitation Rabi frequencies. This measurement is shown in Fig. 8(b) and shows a linear increase of the linewidth as a function of the excitation power. The reason for the additional contribution to the linewidth and its linear broadening with the excitation power requires further investigations.

## IX. SPIN PUMPING AND RABI OSCILLATIONS

Fig. 9(a) shows a measurement of the resonance fluorescence of the negative trion as a function of the gate voltage and the laser wavelength. This measurement is performed on the QD which is presented in Fig. 1(b) of the main text. The trion is stable in the gate voltage range between  $V_g = -0.52$  V and  $V_g = -0.48$  V. This charge plateau splits into two due to the electron spin Zeeman energy. We perform the measurements of the radiative Auger emission on one Zeeman branch. No Zeeman splitting is observed in the emission spectrum, which shows that the radiative Auger process is spin-conserving. In the centre of the charge plateau, the resonance fluorescence disappears due to optical spin pumping. At the edges of the charge plateau, the resonance fluorescence is strong due to spin co-tunneling with the back gate<sup>36,37</sup>. For this reason, we perform all measurements in the co-tunneling regime.

Fig. 9(b) shows resonantly driven Rabi-oscillations as a function of the excitation power. The measurement is performed on the trion state of the same QD. These coherent oscillations in the auto-correlation ( $g^{(2)}$ ) measurement show that the QD can be approximately described by a two-level system<sup>49</sup>. However, radiative Auger is a fundamental process that limits this two-level approximation in the case of a trion.

\* matthias.loebel@unibas.ch

- <sup>1</sup> T. Åberg and J. Utriainen, Phys. Rev. Lett. **22**, 1346 (1969).
- <sup>2</sup> T. Åberg, Phys. Rev. A **4**, 1735 (1971).
- <sup>3</sup> F. Bloch and P. A. Ross, Phys. Rev. **47**, 884 (1935).
- <sup>4</sup> P. Hawrylak, *Single quantum dots: Fundamentals, applications and new concepts*, edited by P. Michler, Vol. 90 (Springer Science & Business Media, 2003).
- <sup>5</sup> W. Bambynek, B. Crasemann, R. W. Fink, H. U. Freund, H. Mark, C. D. Swift, R. E. Price, and P. V. Rao, Rev. Mod. Phys. **44**, 716 (1972).
- <sup>6</sup> M.-G. Barthés-Labrousse, Microscopy Microanalysis Microstructures **6**, 253 (1995).
- <sup>7</sup> J. M. Howard, E. J. Seykora, and A. W. Waltner, Phys. Rev. A **4**, 1740 (1971).
- <sup>8</sup> T. A. Carlson, Phys. Rev. **130**, 2361 (1963).
- <sup>9</sup> A. Kurzmann, A. Ludwig, A. D. Wieck, A. Lorke, and M. Geller, Nano Lett. **16**, 3367 (2016).
- <sup>10</sup> B. Han, C. Robert, E. Courtade, M. Manca, S. Shree, T. Amand, P. Renucci, T. Taniguchi, K. Watanabe, X. Marie, L. E. Golub, M. M. Glazov, and B. Urbaszek, Phys. Rev. X **8**, 031073 (2018).
- <sup>11</sup> P. Siyushev, H. Pinto, M. Vörös, A. Gali, F. Jelezko, and J. Wrachtrup, Phys. Rev. Lett. **110**, 167402 (2013).
- <sup>12</sup> P. Blood, *Quantum Confined Laser Devices: Optical gain and recombination in semiconductors*, Vol. 23 (OUP Oxford, 2015).
- <sup>13</sup> M. S. Skolnick, K. J. Nash, D. J. Mowbray, M. K. Saker, T. A. Fisher, D. M. Whittaker, D. W. Peggs, N. Miura,

- S. Sasaki, R. S. Smith, and S. J. Bass, Solid-State Electronics **37**, 825 (1994).
- <sup>14</sup> M. J. Manfra, B. B. Goldberg, L. Pfeiffer, and K. West, Phys. Rev. B **57**, R9467 (1998).
- <sup>15</sup> N. A. J. M. Kleemans, J. van Bree, A. O. Govorov, J. G. Keizer, G. J. Hamhuis, R. Nötzel, A. Y. Silov, and P. M. Koenraad, Nat. Phys. **6**, 534 (2010).
- <sup>16</sup> Y. H. Huo, A. Rastelli, and O. G. Schmidt, Appl. Phys. Lett. **102**, 152105 (2013).
- <sup>17</sup> R. J. Warburton, C. Schäfflein, D. Haft, F. Bickel, A. Lorke, K. Karrai, J. M. Garcia, W. Schoenfeld, and P. M. Petroff, Nature **405**, 926 (2000).
- <sup>18</sup> J. Hanson, C. H. H. Schulte, C. Matthiesen, M. J. Stanley, and M. Atatüre, Appl. Phys. Lett. **105**, 172107 (2014).
- <sup>19</sup> Z. X. Koong, D. Scerri, M. Rambach, T. S. Santana, S. I. Park, J. D. Song, E. M. Gauger, and B. D. Gerardot, Phys. Rev. Lett. **123**, 167402 (2019).
- <sup>20</sup> A. J. Brash, J. Iles-Smith, C. L. Phillips, D. P. S. McCutcheon, J. O'Hara, E. Clarke, B. Royall, L. R. Wilson, J. Mørk, M. S. Skolnick, A. M. Fox, and A. Nazir, Phys. Rev. Lett. **123**, 167403 (2019).
- <sup>21</sup> L. P. Kouwenhoven, D. G. Austing, and S. Tarucha, Rep. Prog. Phys. **64**, 701 (2001).
- <sup>22</sup> V. Fock, Zeitschrift für Physik **47**, 446 (1928).
- <sup>23</sup> C. G. Darwin, Proc. Camb. Phil. Soc. **27**, 86 (1930).
- <sup>24</sup> B. Ohnesorge, M. Albrecht, J. Oshinowo, A. Forchel, and Y. Arakawa, Phys. Rev. B **54**, 11532 (1996).
- <sup>25</sup> H. Kurtze, J. Seebeck, P. Gartner, D. R. Yakovlev, D. Reuter, A. D. Wieck, M. Bayer, and F. Jahnke, Phys.



- Rev. B **80**, 235319 (2009).
- <sup>26</sup> X.-Q. Li, H. Nakayama, and Y. Arakawa, Phys. Rev. B **59**, 5069 (1999).
  - <sup>27</sup> K. Müller, A. Bechtold, C. Ruppert, T. Kaldewey, M. Zecherle, J. S. Wildmann, M. Bichler, H. J. Krenner, J. M. Villas-Bôas, G. Abstreiter, M. Betz, and J. J. Finley, Ann. Phys. **525**, 49 (2013).
  - <sup>28</sup> M. C. Löbl, I. Söllner, A. Javadi, T. Pregnolato, R. Schott, L. Midolo, A. V. Kuhlmann, S. Stobbe, A. D. Wieck, P. Lodahl, A. Ludwig, and R. J. Warburton, Phys. Rev. B **96**, 165440 (2017).
  - <sup>29</sup> P. M. Vora, A. S. Bracker, S. G. Carter, T. M. Sweeney, M. Kim, C. S. Kim, L. Yang, P. G. Brereton, S. E. Economou, and D. Gammon, Nat. Commun. **6**, 7665 (2015).
  - <sup>30</sup> A. Javadi, D. Ding, M. H. Appel, S. Mahmoodian, M. C. Löbl, I. Söllner, R. Schott, C. Papon, T. Pregnolato, S. Stobbe, L. Midolo, T. Schröder, A. D. Wieck, A. Ludwig, R. J. Warburton, and P. Lodahl, Nat. Nanotechnol. **13**, 398 (2018).
  - <sup>31</sup> J. Q. Grim, A. S. Bracker, M. Zalalutdinov, S. G. Carter, A. C. Kozen, M. Kim, C. S. Kim, J. T. Mlack, M. Yakes, B. Lee, and D. Gammon, Nat. Mater. **18**, 963 (2019).
  - <sup>32</sup> Z. M. Wang, B. L. Liang, K. A. Sablon, and G. J. Salamo, Appl. Phys. Lett. **90**, 113120 (2007).
  - <sup>33</sup> R. B. Patel, A. J. Bennett, I. Farrer, C. A. Nicoll, D. A. Ritchie, and A. J. Shields, Nat. Photonics **4**, 632 (2010).
  - <sup>34</sup> G. Kiršanskė, H. Thyrrerstrup, R. S. Daveau, C. L. Dreeßen, T. Pregnolato, L. Midolo, P. Tighineanu, A. Javadi, S. Stobbe, R. Schott, A. Ludwig, A. D. Wieck, S. I. Park, J. D. Song, A. V. Kuhlmann, I. Söllner, M. C. Löbl, R. J. Warburton, and P. Lodahl, Phys. Rev. B **96**, 165306 (2017).
  - <sup>35</sup> M. Kroutvar, Y. Ducommun, D. Heiss, M. Bichler, D. Schuh, G. Abstreiter, and J. J. Finley, Nature **432**, 81 (2004).
  - <sup>36</sup> J. Dreiser, M. Atatüre, C. Galland, T. Müller, A. Badolato, and A. Imamoglu, Phys. Rev. B **77**, 075317 (2008).
  - <sup>37</sup> J. M. Smith, P. A. Dalgarno, R. J. Warburton, A. O. Govorov, K. Karrai, B. D. Gerardot, and P. M. Petroff, Phys. Rev. Lett. **94**, 197402 (2005).
  - <sup>38</sup> A. V. Madhav and T. Chakraborty, Phys. Rev. B **49**, 8163 (1994).
  - <sup>39</sup> R. J. Warburton, B. T. Miller, C. S. Dürr, C. Bödefeld, K. Karrai, J. P. Kotthaus, G. Medeiros-Ribeiro, P. M. Petroff, and S. Huant, Phys. Rev. B **58**, 16221 (1998).
  - <sup>40</sup> S.-J. Cheng, W. Sheng, and P. Hawrylak, Phys. Rev. B **68**, 235330 (2003).
  - <sup>41</sup> M. C. Löbl, S. Scholz, I. Söllner, J. Ritzmann, T. Denneulin, A. Kovacs, B. E. Kardynał, A. D. Wieck, A. Ludwig, and R. J. Warburton, Commun. Phys. **2**, 93 (2018).
  - <sup>42</sup> J. C. Slater, Phys. Rev. **34**, 1293 (1929).
  - <sup>43</sup> E. U. Condon, Phys. Rev. **36**, 1121 (1930).
  - <sup>44</sup> D. Chithrani, M. Korkusinski, S.-J. Cheng, P. Hawrylak, R. L. Williams, J. Lefebvre, P. J. Poole, and G. C. Aers, Physica E: Low-dimensional Systems and Nanostructures **26**, 322 (2005).
  - <sup>45</sup> J. R. Johansson, P. D. Nation, and F. Nori, Computer Physics Communications **184**, 1234 (2013).
  - <sup>46</sup> J.-P. Jahn, M. Munsch, L. Béguin, A. V. Kuhlmann, M. Renggli, Y. Huo, F. Ding, R. Trotta, M. Reindl, O. G. Schmidt, A. Rastelli, P. Treutlein, and R. J. Warburton, Phys. Rev. B **92**, 245439 (2015).
  - <sup>47</sup> J. Hansom, C. H. H. Schulte, C. Le Gall, C. Matthiesen, E. Clarke, M. Hugues, J. M. Taylor, and M. Atatüre, Nat. Phys. **10**, 725 (2014).
  - <sup>48</sup> R. Loudon, *The quantum theory of light* (OUP Oxford, 2000).
  - <sup>49</sup> E. B. Flagg, A. Muller, J. Robertson, S. Founta, D. Deppe, M. Xiao, W. Ma, G. Salamo, and C.-K. Shih, Nat. Phys. **5**, 203 (2009).



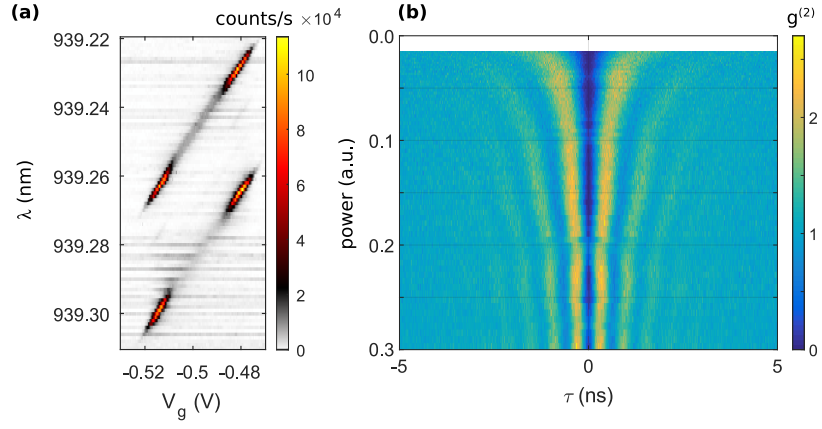


FIG. 9. **(a)** The charge plateau of the resonantly excited trion at a magnetic field of 0.6 T. This measurement is carried out on the InGaAs quantum dot (QD) shown in Fig. 1(b) of the main text. At the edges of the charge plateau, a strong resonance fluorescence is detected. In the plateau center, the resonance fluorescence intensity is strongly reduced due to electron spin pumping. All radiative Auger measurements are performed at the plateau edges. **(b)** Power dependent  $g^{(2)}$ -measurement on the negative trion of the same QD.